Journal of Sol-Gel Science and Technology
https://doi.org/10.1007/s10971-023-06225-4

ORIGINAL PAPER: FUNCTIONAL COATINGS, THIN FILMS AND MEMBRANES (INCLUDING DEPOSITION TECHNIQUES)

# Pulsed laser crystallization of sol-gel derived cerium oxide thin films

Elena Colusso[1] · Maria Basso[1] · Chiara Carraro[2] · Caterina Cesaroni[1] · Enrico Di Russo[2] · Massimo Guglielmi[1] · Enrico Napolitani[2] · Alessandro Martucci[1]

Received: 7 February 2023 / Accepted: 4 September 2023


## Abstract

Cerium oxide sol-gel-derived thin films were crystallized by pulsed excimer laser annealing (ELA). X-ray diffraction (XRD), scanning electron microscopy (SEM), Raman Spectroscopy (RS), and Fourier transform infrared (FTIR) were employed to analyze the effect of laser fluence and number of pulses on the structural and morphological properties of the irradiated films. XRD and RS results, supported by thermal simulations, confirmed crystallization into cubic cerium oxide starting from 40 mJcm$^{-2}$. SEM micrographs showed that an increased number of pulses induced the formation of porous and complex nanostructured surfaces, different from the morphology obtained on thermally annealed films. Finally, water contact angle measurements revealed that the films showed a characteristic hydrophobic "petal effect".

## Graphical Abstract

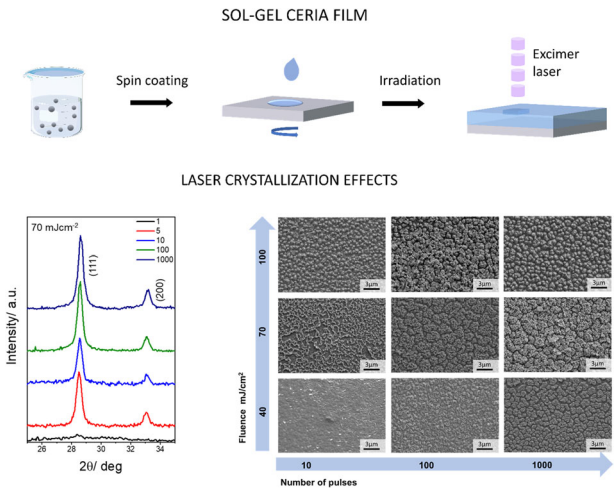


**Keywords** cerium oxide · sol-gel · excimer laser · photonic curing · nanostructuring

## Highlights

- Successful crystallization of cubic cerium oxide films by pulsed laser annealing
- Effect of laser fluence, number of pulses and film thickness was investigated
- Characterization of the surface morphology evolution was performed by FE-SEM

✉ Alessandro Martucci
alex.martucci@unipd.it

[1] Department of Industrial Engineering and INSTM, University of Padova, Via Marzolo 9, Padova 35131, Italy

[2] Department of Physics and Astronomy and LNL-INFN, University of Padova, Via Marzolo 8, Padova 35131, Italy

Published online: 27 September 2023

## 1 Introduction

Solution-based approaches such as sol-gel, chemical bath deposition and metal-organic decomposition have been widely investigated for the fabrication of functional metal oxide thin films [1, 2]. Conventional procedures involve the deposition onto substrates by spin, dip or spray coating followed by thermal annealing of the film. The temperature reached for crystallization is sometimes incompatible with inexpensive and temperature-sensitive substrates. Laser annealing of a thin film is emerging as an alternative technique for rapid crystallization at room temperature, with the advantages of fast processing and scalability, along with precise control of the irradiated area, surface morphology, and in-depth thermal profile by tuning the laser parameters [3].

Crystallization of sol-gel metal-oxides by an excimer laser has been already reported [4–7]. Dellis et al. demonstrated the crystallization of indium oxide films induced by photochemical conversion and their potential application in thin-film transistors [8]. Tsay et al. investigated the effect of energy density on the electrical properties of InGaZnO films at a fixed number of pulses (15) [9]. Several authors explored the laser annealing of zinc oxide and doped zinc oxide films on glass substrates [5, 6, 10]. Other groups fabricated mesoporous titania and titania-doped films with multiphase structures depending on the processing conditions for potential application in photocatalysis [4].

Among the metal oxides, cerium dioxide ($CeO_2$) has attracted attention for its unique properties, including high oxygen storage capacity, excellent lattice match and similar thermal expansion coefficient to silicon, high refractive index and band gap values, electrochromism, transparency in the VIS-NIR regions with high thermal and chemical stability, hydrophobicity, non-toxicity, antibacterial activity and antioxidant activity [11, 12]. It has found a wide range of applications, ranging from sensing, optics, catalysis, corrosion resistance and protective coatings, smart windows and electrochromic displays, and medicine [11–15].

Several techniques have been reported for the fabrication of cerium oxide thin films, including magnetron sputtering, atomic layer deposition, electron-beam, spray pyrolysis, pulsed laser deposition, chemical deposition and sol-gel [16–19]. Regarding the sol-gel process, several works report the synthesis of cerium oxide films. Ansari et al. developed a nanoporous film on indium-tin-oxide-coated glass for cholesterol biosensors [20]. Ceria thin films prepared using an ethanolic precursor sol containing cerium chloride and citric acid by dip coating technique were reported by Gökdemir et al. [21]. Acosta-Silva et al. investigated the effect of annealing temperature on the morphological, structural and optical properties of cerium oxide sol-gel films prepared by spin coating [22].

Here, we explored the effect of Excimer Laser Annealing (ELA) using a pulsed KrF (248 nm) laser on the microstructural and morphological evolution of sol-gel cerium oxide thin films prepared from a cerium nitrate ethanolic solution. To the best of our knowledge, this is the first report on the use of laser irradiation on cerium-derived sol-gel films. We demonstrated that pulsed laser irradiation induces rapid crystallization of cubic cerium oxide and generates unique nanostructured topographies, which can be exploited for the fabrication of wettability gradient surfaces, gas sensors or nano-porous layers for catalysis [15, 23, 24]. We studied the influence of irradiation parameters on the microstructure, surface morphology and wettability of thin films by employing X-ray diffraction, Raman spectroscopy, scanning electron microscopy and water contact angle measurements. Simple numerical simulations were performed to estimate the temperature gradient along the film thickness.

## 2 Experimental

### 2.1 Materials

Cerium nitrate hexahydrate ($Ce(NO_3)_3 \cdot 6H_2O$, Aldrich, 98%), absolute ethanol (EtOH, Sigma-Aldrich), citric acid monohydrate (CA, ACS reagent, ≥99.0%, Sigma-Aldrich), ethylene glycol (EG, anhydrous, 99.8%, Sigma-Aldrich).

### 2.2 Preparation of CeO2 precursor solution

A cerium-based solution was prepared following a sol-gel approach adapted from the literature [21, 22]. Briefly, $Ce(NO_3)_3 \cdot 6H_2O$ was dissolved in EtOH with a molar ratio with respect to the solvent of 1:50. Separately, a second solution of citric acid and ethylene glycol in ethanol was prepared (molar ratio 1:1:50 CA:EG:EtOH). Both solutions were kept under stirring for 30 min at room temperature and then mixed together. The final solution was stirred for 1 h at room temperature before the deposition.

### 2.3 Preparation of CeO2 thin films

Thin films were deposited on silicon wafers (5 × 5 cm) by spin coating. Before the coating, substrates were cleaned by sonication in ethanol, followed by sonication in acetone, and blown dry with $N_2$. Then the surfaces were treated with air plasma (model PDC-32 G-2; Harrick Plasma, Ithaca, NY) for 2 min. Coatings with a tunable thickness were deposited by sequential spin coating deposition. A first spin cycle was at 500 rpm for 3 s and a second at 2000 rpm for 30 s. Immediately after the deposition, the films were submitted to a heat treatment at 300 °C for 10 min for each

deposited layer. Samples with 1 layer (1L_$CeO_2$) or 5 layers (5L_$CeO_2$) were prepared with this protocol. The as-deposited films were treated with an excimer laser at different fluences or annealed in an oven at different temperatures (500–1000 °C, heating rate 10 °C/min) for 1 h as a reference.

### 2.4 Excimer laser annealing

The as-deposited films were irradiated with a KrF laser (248 nm, Coherent - Compex PRO 201 F) at fluence values of 40, 70, 100 mJ/cm$^2$ for 1, 5, 10, 100 or 1000 pulses, that lasted 22 ns at a repetition rate of 10 Hz. For each condition, an area of the films of $10 \times 5$ mm$^2$ with <2% uniformity was irradiated in air.

### 2.5 Characterization

The crystalline structure of the films was evaluated by glancing angle X-ray diffraction (Philips PW1710 diffractometer), using a 2° incidence angle and CuKα radiation at 30 kV and 30 mA. Crystalline phases were identified by using the software Match! Diffraction Analysis and the crystallite size ($D$) was determined by using the Scherrer equation, $D = (K\lambda/\beta cos\theta)$, where $K$ is the Scherrer constant ($K = 0.94$), $\lambda$ is the wavelength of the incident X-ray ($\lambda = 0.15401$ nm), $\beta$ is the full width at half-maximum intensity of the 111 peak, and $\theta$ is the Bragg diffraction angle ($2\theta = 28.5°$).

The morphology of the samples was examined using field-emission scanning electron microscopy (FE-SEM, Zeiss Sigma HD) operating at 5 kV and collecting signals by means of a secondary electron detector. Some samples were mechanically fractured for cross-section images. All the samples were observed as prepared without further modification of the surface.

Thickness and optical constants (n and k) of the as-deposited film were determined by ellipsometry (Woollam Co., WVase 32). Measurements were conducted at two angles of incidence (65°–75°), in the 280–1200 nm wavelength range. For data analysis, a model of the measured sample was created using a layer of silicon as substrate and a GENOSC layer for the cerium oxide film with a Tauch-Lorentz oscillator. Reflection and absorption coefficient at 248 nm for the simulations were generated by using the Woolam software, starting from the model created.

FTIR spectra of the samples were collected in transmission mode with a Jasco FT-IR 4200, in the 4500–400 cm$^{-1}$ range, at 64 scans min$^{-1}$ and with a resolution of 4 cm$^{-1}$, by collecting the background on a bare silicon substrate.

Raman spectra were collected using a Horiba XploRA™ Plus System with a 532 nm laser through a 50× magnification objective. Each spectrum was acquired in the 200–800 cm$^{-1}$ range by averaging 10 consecutive exposures with an integration time of 2 s each. The contribution from the silicon substrate at 521 cm$^{-1}$ was excluded from the spectra.

Dynamic contact angles (advancing and receding) were measured by the addition-removal method, by dispersing and withdrawing a water droplet of about 5 µl volume. The measurements were conducted with a home-made set-up consisting of a dispersing microfluidic syringe, a sensor camera (DCC1545M CMOS, Thorlabs GmbH®, Bergkirchen, Germany) and sensor lens (MVL7000, Thorlabs GmbH®, Bergkirchen, Germany).

### 2.6 Numerical simulations

Simulations of thermal profiles as a function of time were performed by numerical solutions of the heat equation. Heat flow calculations were performed by employing the LIMP software (Laser Induced Melting Prediction), the Harvard simulation software package and calibrated on $CeO_2$ and silicon optical and physical data. The former were extrapolated from ellipsometry measurements performed in this work, while the latter were obtained from the literature [25].

## 3 Results

Cerium-based sol-gel films were deposited on silicon substrates by a multilayer spin-coating deposition (1 and 5 layers), according to the protocol reported in the Experimental section. The films were dried at 300 °C for 10 min before the following deposition to ensure solvent evaporation and stabilization of the layers. The final thickness of the 1L_$CeO_2$ and 5L_$CeO_2$ film were about $170 \pm 10$ and $510 \pm 15$ nm, respectively, as measured by ellipsometry. Samples were then irradiated with the pulsed KrF excimer laser. Different combinations of laser fluences (40, 70, 100 mJcm$^{-2}$) and number of pulses (1, 5, 10, 100, 1000) were exploited to analyze the influence on the formation of crystalline cerium oxide. Thermal crystallization of the prepared xerogels was confirmed by X-ray diffraction analysis on samples annealed in a furnace at 500 °C and 1000 °C (Fig. S1).

### 3.1 X-ray diffraction analysis

Figures 1 and 2 show the X-ray diffraction patterns of the different samples irradiated with ELA compared to the as-prepared ones. According to XRD analysis, the dried samples (Figs. 1a and 2a) were amorphous. A single pulse did not lead to crystallization in any of the fluences considered for 1- and 5-layer samples. By increasing the number of pulses, diffraction peaks appear at 28.5° and 33.1°, that

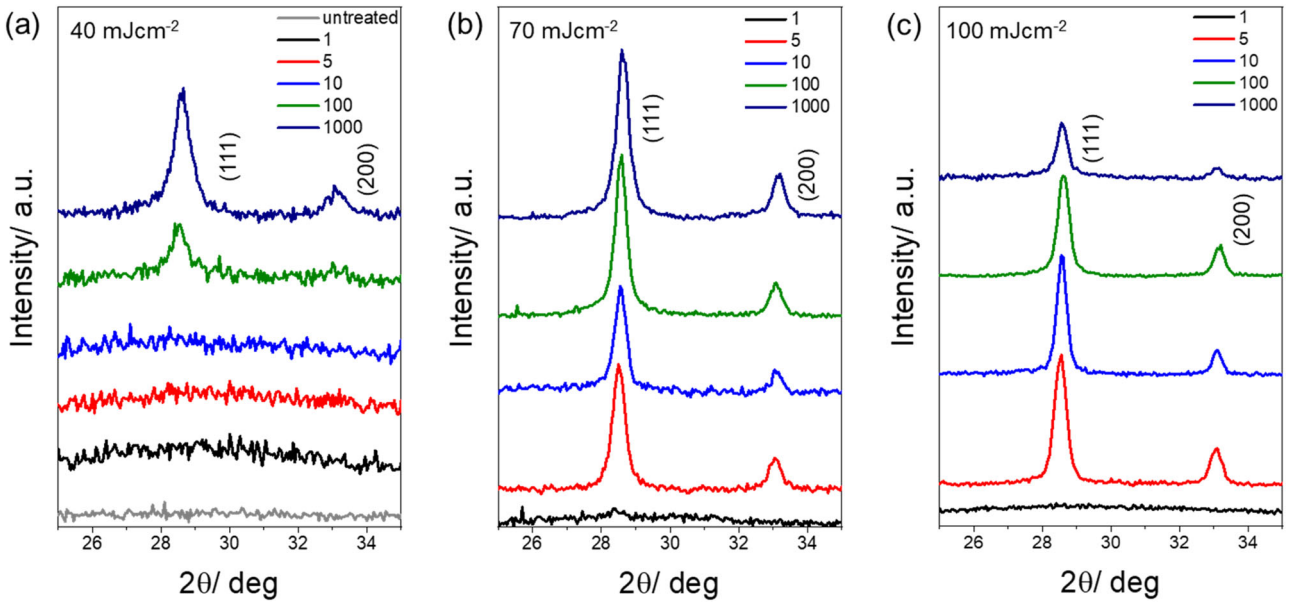


**Fig. 1** (111) and (200) diffraction peaks of 5L_$CeO_2$ films prepared on silicon substrates after pulses excimer laser annealing as a function of number of pulses (1, 5, 10, 100 and 1000 pulses) at varies laser fluences: 40 $mJcm^{-2}$ (**a**), 70 $mJcm^{-2}$ (**b**), and 100 $mJcm^{-2}$ (**c**). The diffractogram of the untreated sample is reported as reference

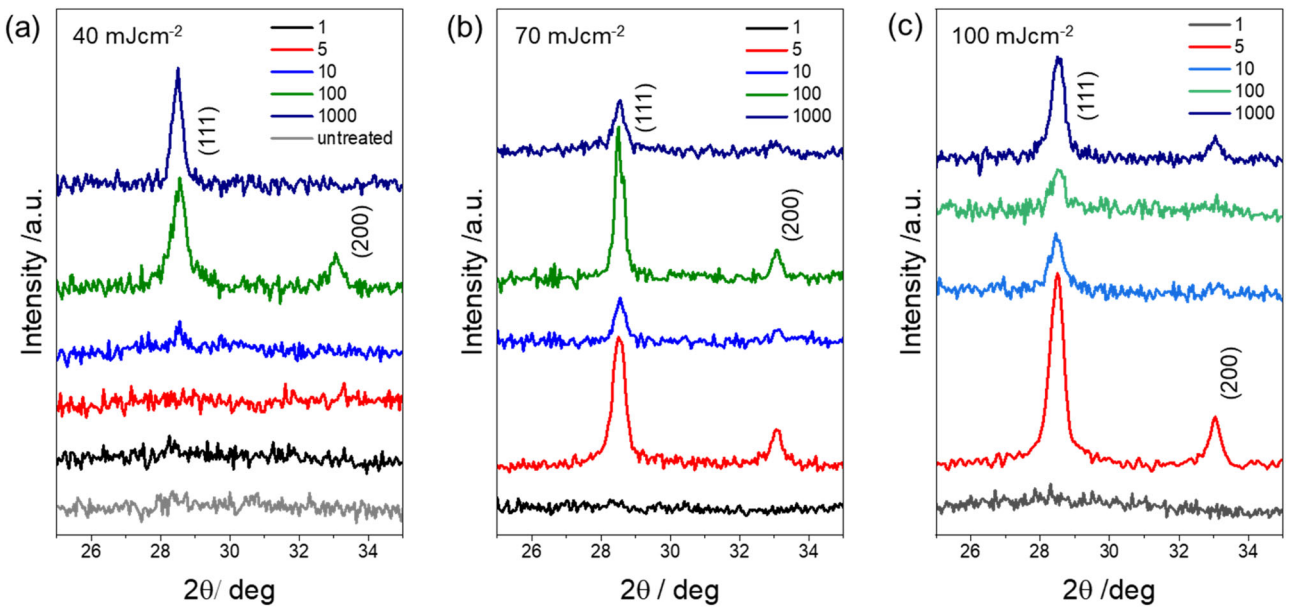


**Fig. 2** (111) and (200) diffraction peaks of 1L_$CeO_2$ films prepared on silicon substrates after pulses excimer laser annealing as a function of number of pulses (1, 5, 10, 100 and 1000 pulses) at varies laser fluences: 40 $mJcm^{-2}$ (**a**), 70 $mJcm^{-2}$ (**b**), and 100 $mJcm^{-2}$ (**c**). The diffractogram of the untreated sample is reported as reference in (**a**)

correspond respectively to the (111) and (200) reflections of cubic $CeO_2$ (JCPDS #43-1002). Concerning the influence of pulses, a different behavior was observed among all the samples depending on the laser fluence considered.

In the case of the 5 L_$CeO_2$, at an energy density of 40 $mJcm^{-2}$, a number of pulses ≥100 was found to be necessary for the formation of crystalline cerium oxide. At higher fluences (70–100 $mJcm^{-2}$), diffraction peaks appear after only 5 pulses.

A similar trend is shown in the diffraction patterns of 1L_$CeO_2$ films (Fig. 2). However, a weak peak at 28.5° appears at 40 $mJcm^{-2}$ and 10 pulses, corresponding to the emerging cubic phase. Compared to the thicker 5L samples, the higher signal noise of the 1L_$CeO_2$ patterns should be considered. This is likely due to the morphology of the films after the laser irradiation, as we will discuss later.

The average crystallite size diameter among all the samples was estimated between 17 and 28 nm (see Table S1). No clear

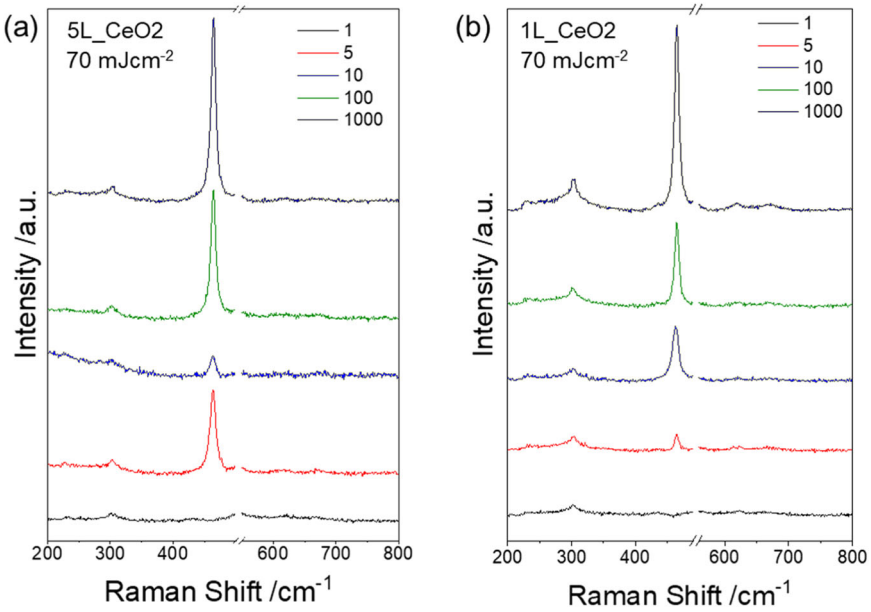


**Fig. 3** Raman spectra of 5L_$CeO_2$ (**a**) and 1L_$CeO_2$ (**b**) films on silicon substrates after pulses excimer laser annealing as a function of number of pulses (1, 5, 10, 100 and 1000 pulses) at 70 $mJcm^{-2}$ laser fluence

relations between the average size and the fluence or pulses could be determined. However, we can observe that the crystallite size is generally higher than that calculated for the thermally treated samples, which was in the 6–7 nm range for samples annealed at both 500 °C and 1000 °C. Similar values were obtained by sol-gel processes using the cerium nitrate precursor [22]. In general, the increase in crystallite size during laser annealing is caused by a local increase in annealing temperature. The decrease at higher fluences has been explained by laser ablation phenomena, which introduces defects and grain boundaries [26].

### 3.2 Raman spectroscopy

The crystallization of $CeO_2$ films after ELA was further confirmed by Raman Spectroscopy. Figure 3 shows the Raman spectra of 5L_$CeO_2$ and 1L_$CeO_2$ treated at 70 $mJcm^{-2}$ with a different number of pulses, measured in the 300–800 $cm^{-1}$ range. The peak at 300 $cm^{-1}$ is due to the Si (100) substrate [27]. The peak near 464 $cm^{-1}$, which appears after 5 pulses, is associated with the $F_{2g}$ Raman active mode of crystalline cubic $CeO_2$ [27, 28]. The same characteristic peak is evident in the thermally annealed sample (Fig. S1b). No peaks are present in the spectra of the pristine samples and in the 1 pulse-ELA, due to negligible crystallization in accordance with XRD results. The position of the peak shifted between 463–465 $cm^{-1}$, as the number of pulses increased from 5 to 1000. Moreover, the full width at half maximum (FWHM) of the $F_{2g}$ band decreases on ELA samples compared to the thermally annealed films (see Table S1). This is associated with an increase in particle size [29, 30], as already determined by XRD. The weak peaks at 600 and 670 $cm^{-1}$ in the samples treated with 1000 pulses could be attributed to oxygen vacancies [29, 30], although they could also be related to second order Raman features [31].

### 3.3 FTIR characterizations

FTIR measurements were carried out to investigate the chemical evolution of the coatings after the treatments. Figure 4 show the FTIR spectra of the coatings as-prepared, after conventional thermal annealing (500 °C) and photonic curing at 100 $mJcm^{-2}$ and 5 pulses.

The spectra of the pristine samples show a pronounced band at 3500–3400 $cm^{-1}$, attributed to the -OH stretching vibration belonging to the hydrated species, such as physisorbed $H_2O$ or from surface Ce–OH groups. Another vibrational contribution of adsorbed water is also observed at 1640 $cm^{-1}$. The band in the range 1400–1700 $cm^{-1}$ can be assigned to the residual nitrate groups from the precursor [32]. Furthermore, there is a possible overlap at 1700 $cm^{-1}$ with the vibrational mode from the C = O bond in the ester groups formed during the reaction between the $^-$COOH groups in citric acid and -OH groups in alcohol. The peaks are attenuated after 5 pulses of ELA at 100 $mJcm^{-2}$ and disappear after calcination at 500 °C. The band below 800 $cm^{-1}$ corresponds to Ce–O vibrations in $CeO_2$ crystals [21]. The peak at 900 $cm^{-1}$ is assigned to C-H deformation, while the band at 1100 $cm^{-1}$ could be assigned to C-O stretching vibrational modes. The FTIR spectra confirm the formation of cerium oxide bonds and the removal of residual groups during the annealing.

### 3.4 Surface morphology

The surface morphology of the as-prepared samples after ELA are shown in Figs. 5 and 7. As seen from the top-view

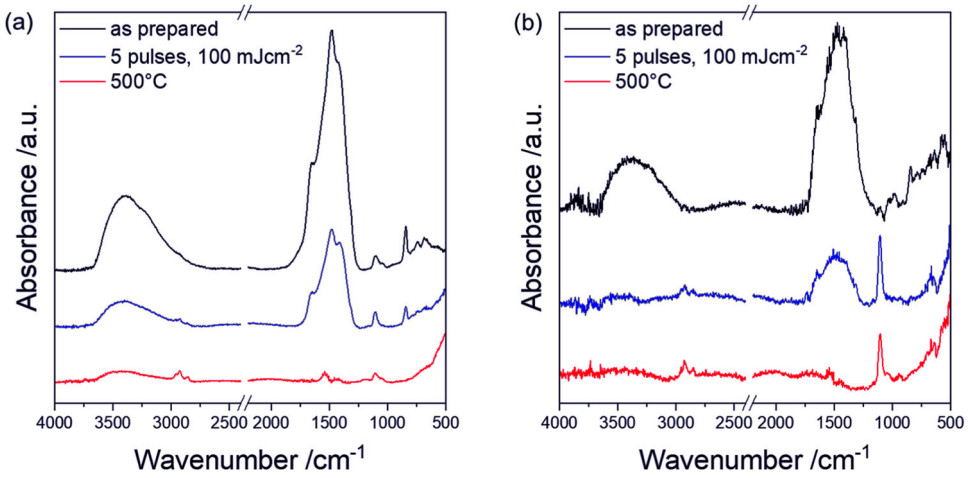


**Fig. 4** FTIR spectra of 5L_$CeO_2$ film (**a**) and 1L_$CeO_2$ (**b**) films as prepared and after different annealing treatments

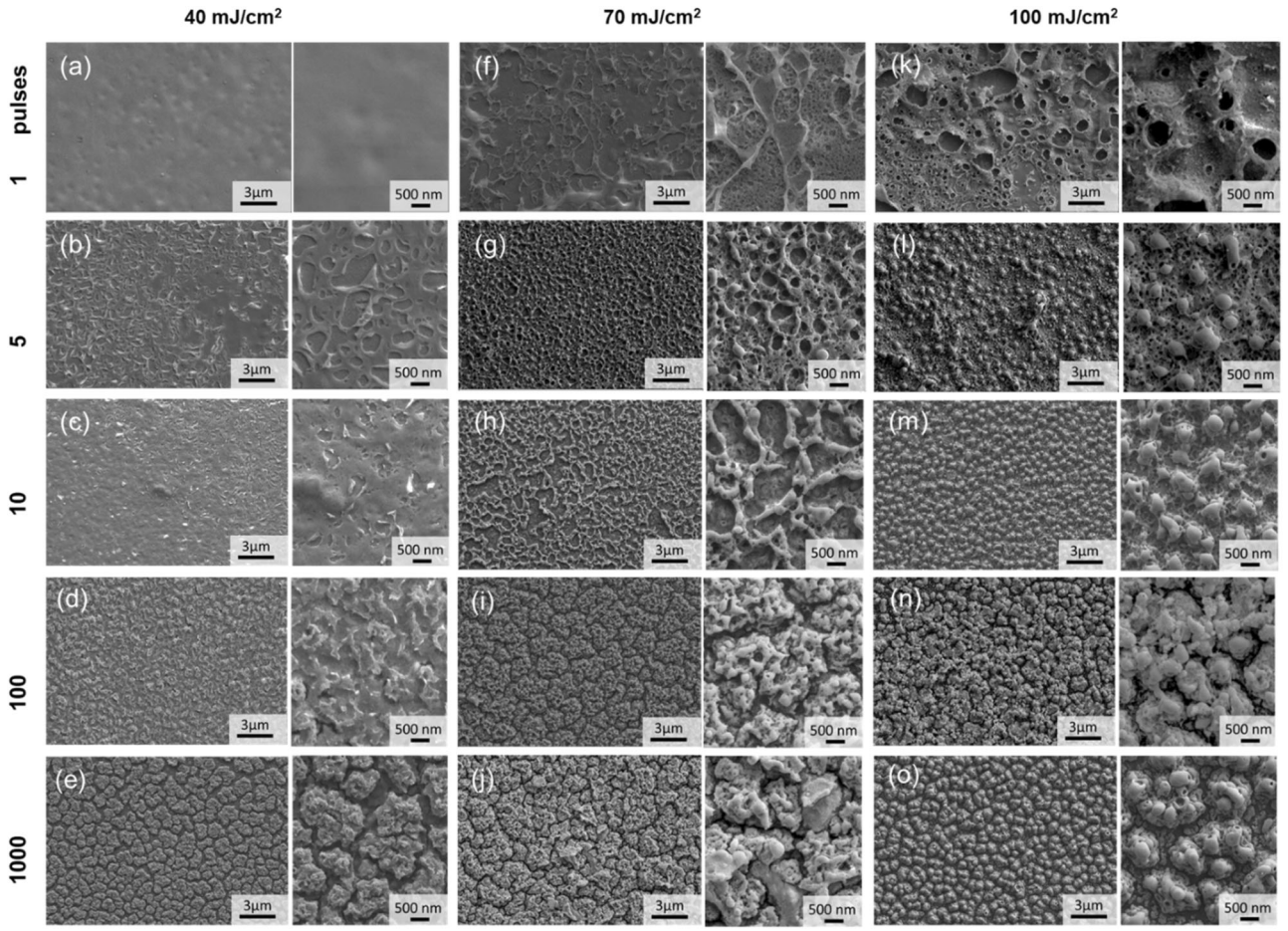


**Fig. 5** FE-SEM images of the surface morphology of 5L_$CeO_2$ films prepared by excimer laser irradiation under different conditions: **a** 40 mJcm$^{-2}$and 1 pulse; **b** 40 mJcm$^{-2}$and 5 pulses; **c** 40 mJcm$^{-2}$and 10 pulses; **d** 40 mJcm$^{-2}$ and 100 pulses; **e** 40 mJcm$^{-2}$ and 1000 pulses; **f** 70 mJcm$^{-2}$and 1 pulse; **g** 70 mJcm$^{-2}$ and 5 pulses; **h** 70 mJcm$^{-2}$ and 10 pulses; **i** 70 mJcm$^{-2}$ and 100 pulses; **j** 70 mJcm$^{-2}$ and 1000 pulses; **k** 100 mJcm$^{-2}$ and 1 pulse; **l** 100 mJcm$^{-2}$ and 5 pulses; **m** 100 mJcm$^{-2}$ and 10 pulses; **n** 100 mJcm$^{-2}$ and 100 pulses; **o** 100 mJcm$^{-2}$ and 1000 pulses

FE-SEM micrographs in Fig. S2, the surfaces of the as-prepared 1L_$CeO_2$ and 5L_$CeO_2$ before irradiation are quite smooth and without cracks.

After laser irradiation, the FE-SEM images reveal a gradual evolution of the morphology and roughness that depends on the laser fluence and the number of pulses.

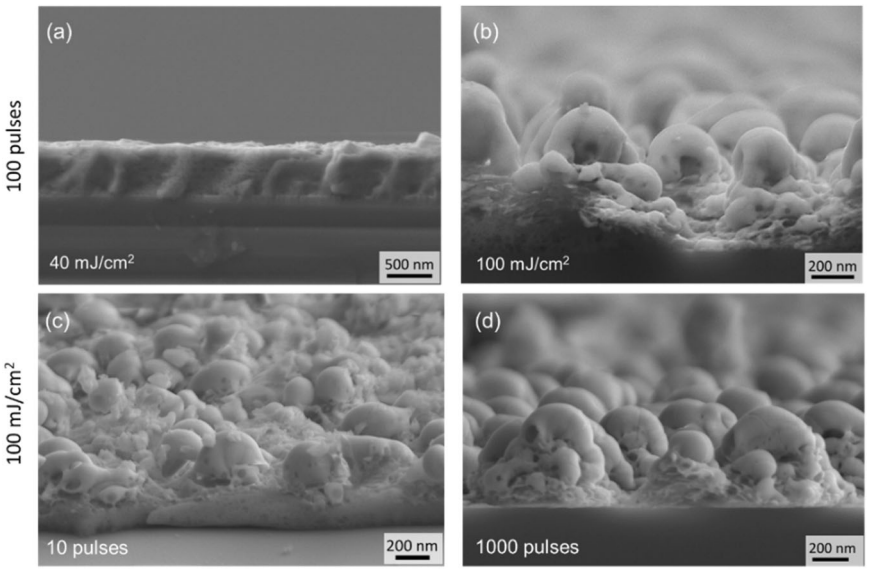


**Fig. 6** Cross-sectional view of the FESEM image of the 5L_$CeO_2$ samples prepared at 40 $mJcm^{-2}$ (**a**) and 100 $mJcm^{-2}$ (**b**) for 100 pulses and at 100 $mJcm^{-2}$ for 10 (**c**) and 1000 (**d**) pulses

Considering a 5L_$CeO_2$ film (Fig. 5a), a single pulse at 40 $mJcm^{-2}$ causes an increase in rugosity with the formation of an "orange peel" texture on the surface. By increasing the energy density (Fig. 5f, k), or the number of pulses to 10 (5b and 5c), while maintaining constant fluence, the surface is gradually transformed into a porous network. At 100 pulses the microstructure of the surface appears to be formed by micrometer rough areas separated by cracks (5d and e), that do not extend through the thickness of the sample, as shown in a characteristic cross-section image in Fig. 6a.

The rise of the laser energy to 70 $mJcm^{-2}$ emphasized the transformation of the surface from a branched network morphology (Fig. 5g, h) to rough isolated islands (Fig. 5I, j). Nanospheres appear on the surfaces as seen in the high-magnification images. The evolution of these morphologies into more spherical and isolated nanostructures is shown when the samples are irradiated at 100 $mJcm^{-2}$.

These features have a dimension of 300–600 nm in length (Fig. 5l–o and Fig. S2) and 600–700 nm in height (Fig. 6b–d). Looking at the cross-section images in Fig. 6, we can observe that these nanostructures are developed throughout the overall film thickness only for ≥100 pulses. They have a characteristic blob-like shape, with nanopores and cracks on the surface (Fig. S3). The formation of cracks is likely due to degradation of residual chemical groups of the precursors, as confirmed by FTIR spectra of the films before irradiation. Indeed, cracks were noticed on corresponding thermally annealed samples (see Fig. S2d). The formation of pores or cracks on solution-processed cerium oxide films was attributed to shrinkage during drying, caused by the removal of hydrate species, and the increasing degree of crystallization [33]. Simonenko et al. reported the formation of more textured coatings as well as an increase in the size of pores between agglomerates with increasing calcination temperature in sol-gel $CeO_2$–$Y_2O_3$ [34]. Islands or bubbles were already observed after KrF irradiation of solution-derived oxide films [26], while ball-like shapes were formed by ELA of crystalline ZnO nanorods [6].

For 1L_$CeO_2$ no variation in the morphology was observed after 1 pulse at 40 $mJcm^{-2}$ (Fig. 7a). Increasing the number of pulses up to 10 (7b-c) or the energy density (7f-k) causes the formation of holes in the films and partial exfoliation of the layer, as observed for the 5L_$CeO_2$. In all the other conditions considered, spherical particles appear on the top surface (Fig. 8). Interestingly, the same morphology consisting of randomly distributed nanoparticles was obtained for 70 and 100 $mJcm^{-2}$ with ≥10 pulses. The nanoparticles have an average diameter of 130–170 nm and they are hollow, as detailed in a characteristic SEM image in Fig. S4. Considering both the results of XRD and SEM, we can define a threshold condition of 70 $mJcm^{-2}$ and 5 pulses for the formation of crystalline nanoparticle patterns in the case of 170 nm thick films.

### 3.5 Numerical simulations of thermal profiles

Because of the extremely short width (22 ns) of the laser pulse, it is complex to quantify the exact surface temperature and temperature profile distribution across the films. Numerical simulations were performed to estimate the heat distribution and the maximum temperature reached at the different laser fluences during a single pulse. It is worth noting that the literature offers a broad range of values depending on the processing conditions. More details about the parameters employed are reported in the Experimental and in Tables S3 and S4 in the SI. Figure 9 shows the simulated temperature profiles for 5L_$CeO_2$ (500 nm thick) and 1L_$CeO_2$ (170 nm thick).

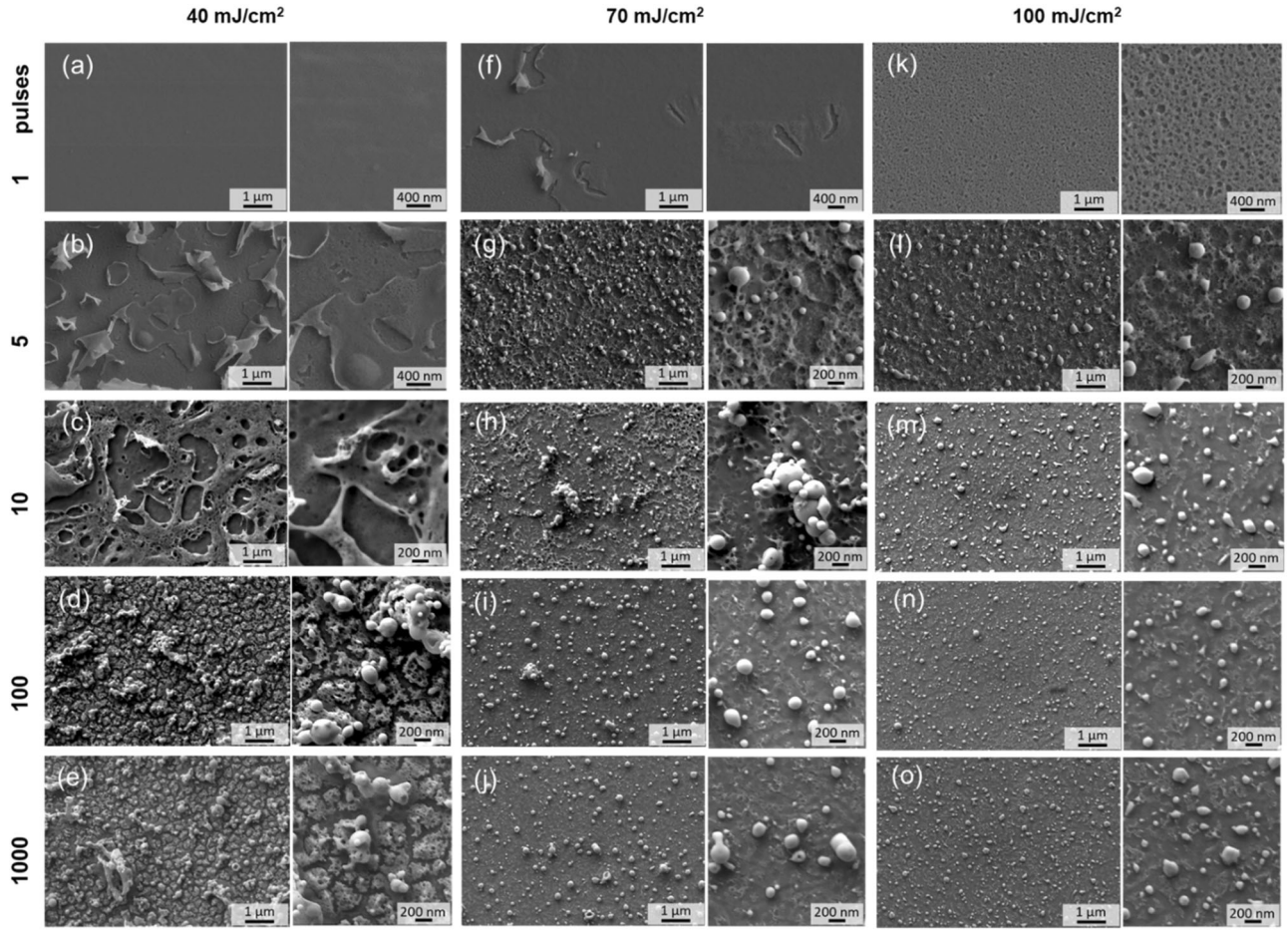


**Fig. 7** FESEM images of the surface morphology of 1L_$CeO_2$ films prepared by excimer laser irradiation at different conditions: **a** 40 $mJcm^{-2}$and 1 pulse; **b** 40 $mJcm^{-2}$and 5 pulses; **c** 40 $mJcm^{-2}$and 10 pulses; **d** 40 $mJcm^{-2}$ and 100 pulses; **e** 40 $mJcm^{-2}$ and 1000 pulses; **f** 70 $mJcm^{-2}$and 1 pulse; **g** 70 $mJcm^{-2}$ and 5 pulses; **h** 70 $mJcm^{-2}$ and 10 pulses; **i** 70 $mJcm^{-2}$ and 100 pulses; **j** 70 $mJcm^{-2}$ and 1000 pulses; **k** 100 $mJcm^{-2}$ and 1 pulse; **l** 100 $mJcm^{-2}$ and 5 pulses; **m** 100 $mJcm^{-2}$ and 10 pulses; **n** 100 $mJcm^{-2}$ and 100 pulses; **o** 100 $mJcm^{-2}$ and 1000 pulses

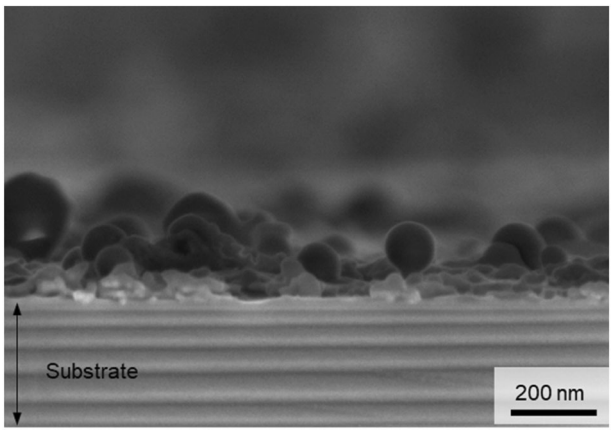


**Fig. 8** Cross-sectional view of FE-SEM image of 1L_$CeO_2$ sample laser irradiated at 40 $mJ/cm^2$ for 100 pulses

As is evident from the profiles, the maximum temperatures reached after a single pulse at the film surfaces for a 510 nm thick film (Fig. 9a) are in the range 300–700 °C, respectively 300 °C (40 $mJcm^{-2}$), 550 °C (70 $mJcm^{-2}$) and 800 °C (100 $mJcm^{-2}$). The fast process causes a large temperature gradient between the film surface and film/substrate interface, with surface-interface differences ranging from 250 °C (40 $mJcm^{-2}$) to a maximum of 700 °C (100 $mJcm^{-2}$). Indeed, the maximum temperature reached by the film/substrate interface after 22 ns is about 54 °C (40 $mJcm^{-2}$), 76 °C (70 $mJcm^{-2}$) and 97 °C (100 $mJcm^{-2}$).

When the thickness is reduced to about 170 nm (Fig. 9b), the temperature differences along the thickness are significantly lower (80–245 °C). At the film/substrate interface, the calculated temperatures are higher, being respectively 120 °C (40 $mJcm^{-2}$), 200 °C (70 $mJcm^{-2}$) and 282 °C (100 $mJcm^{-2}$), while at the film surface they are lower, 200 °C (40 $mJcm^{-2}$), 350 °C (70 $mJcm^{-2}$) and 530 °C (100 $mJcm^{-2}$). This is the result of the direct heating of the Si substrate due to the laser penetration depth (about 200 nm) larger than the film, and the fast heat dissipation through the Si substrate.

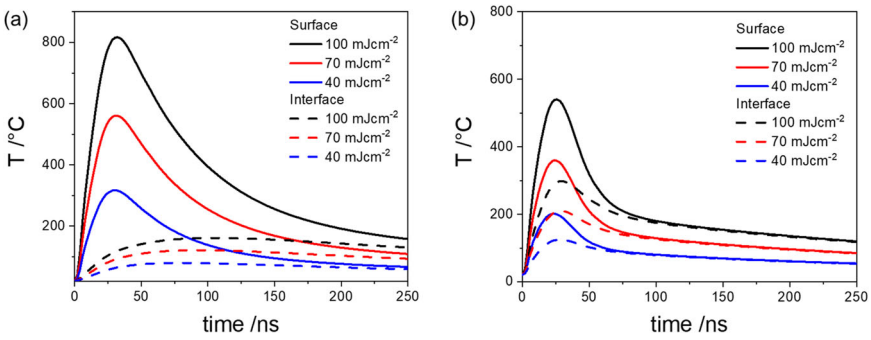


**Fig. 9** Temperature profiles of 5L_$CeO_2$ film (**a**) and 1L_$CeO_2$ (**b**) on silicon substrate. The simulated fluences are 40, 70 and 100 mJ/$cm^2$. Solid and dashed lines respectively indicate the temperature at the film surface and at the film/substrate interface

**Table 1** Advancing (Adv) and receding (Rec) water contact angles of 5L_$CeO_2$ films as-prepared, heat treated at 500 °C and laser irradiated at different laser fluences (40, 70, 100 mJcm$^{-2}$) and number of pulses (10, 100, 1000)

| Sample | Adv (°) | Rec (°) |
|---|---|---|
| Silicon substrate | 56 | 42 |
| As-prepared | 98 | 67 |
| 500 °C | 104 | <5 |
| 40mJcm$^{-2}$-10pulses | 104 | <5 |
| 40mJcm$^{-2}$-100pulses | 115 | <5 |
| 40mJcm$^{-2}$-1000pulses | 140 | <5 |
| 70mJcm$^{-2}$-10pulses | 115 | <5 |
| 70mJcm$^{-2}$-100pulses | 129 | <5 |
| 70mJcm$^{-2}$-1000pulses | 141 | <5 |
| 100mJcm$^{-2}$-10pulses | 141 | <5 |
| 100mJcm$^{-2}$-100pulses | 136 | <5 |
| 100mJcm$^{-2}$-1000pulses | 105 | <5 |

**Table 2** Advancing (Adv) and receding (Rec) water contact angles of 1L_$CeO_2$ films as prepared, heat treated at 500 °C and laser irradiated at different laser fluences (40, 70, 100 mJcm$^{-2}$) and number of pulses (10, 100, 1000)

| Sample | Adv (°) | Rec (°) |
|---|---|---|
| Silicon substrate | 56 | 42 |
| As-prepared | 73 | <5 |
| 500 °C | 113 | 73 |
| 40mJcm$^{-2}$-10pulses | 120 | <5 |
| 40mJcm$^{-2}$-100pulses | 112 | <5 |
| 40mJcm$^{-2}$-1000pulses | 130 | <5 |
| 70mJcm$^{-2}$-10pulses | 102 | <5 |
| 70mJcm$^{-2}$-100pulses | 117 | 56 |
| 70mJcm$^{-2}$-1000pulses | 130 | 50 |
| 100mJcm$^{-2}$-10pulses | 105 | 54 |
| 100mJcm$^{-2}$-100pulses | 117 | 60 |
| 100mJcm$^{-2}$-1000pulses | 122 | 40 |

It was already reported that the crystallization of sol-gel cerium oxide starts between 200–500 °C, depending on the processing conditions [22]. The simulated temperatures at the interface were close to or above the crystallization temperature, but they do not correspond to the XRD results for a single pulse. The differences could be explained by considering the large temperature gradient generated between the surface and interface, and the extremely rapid heating cycle. The short duration of the single pulse could be insufficient to initiate crystallization of the films. The formation of very small crystallite seeds, not detected by XRD analysis, cannot be excluded [3, 7]. However, if we considered an increased number of pulses not accounted for in the simulations, an agreement with diffraction results could be found since crystallization occurs preferentially for fluences ≥70 mJcm$^{-2}$.

## 3.6 Surface wettability

The wettability of 5 L_$CeO_2$ and 1L_$CeO_2$ films was evaluated through advancing/receding contact angle measurements (see Table 1 and Table 2). The as-prepared 1_layer sample shows a hydrophilic behavior with an advancing contact angle of 73° and no receding contact angle. On the contrary, the 5L sample presents a hydrophobic surface with an advancing contact angle of 98° and a hysteresis (defined as the difference between the advancing and receding contact angle) of 31°. The hydrophobicity is consistent with the densification of the sol-gel layer due to the repeated annealing at 300 °C. By firing the samples at 500 °C, an increase in hydrophobicity is observed for the thinner one, with an advancing/receding contact angle of 113°/73°. Similarly, the advancing angle of 5L_$CeO_3$ evolved to 104°, but no receding was measured. This effect is likely due to the presence of cracks on the surface, as shown in the SEM images, that could induce a pinning of the water droplets.

The ELA process induces a significant increase in the advancing contact angle for all the conditions investigated, with a value ranging from 104° to 130°. These values are comparable with the literature, and they are associated with crystallization along the (111) orientation and the surface roughness of the films [35]. Indeed, the water contact angle on

the (111) surface has been reported to be greater than that on the (110) surface [36]. Adsorption of hydrocarbons on the surface, which could contribute to the hydrophobicity, cannot be excluded [37]. On the contrary, by considering the receding contact angle, differences could be noticed between the samples. In particular, all the 5_$CeO_2$ ELA films show no receding, with high adhesion of water droplets as also visible in a representative video (Video S1, SI). This behavior, known as the "petal effect", is attributed to the presence of a wetting composite-Cassie-Baxter state, in which the liquid only partially penetrates and wets the gaps between the pillars while suspended atop the nanoscale features [38].

## 4 Discussion

This work investigated the effect of KrF excimer laser annealing on the microstructure evolution of sol-gel cerium oxide films. The X-ray diffraction measurements enable changes in the $CeO_2$ films to be observed as a function of laser fluence and the number of pulses. We found a threshold condition for the crystallization of the cubic $CeO_2$ phase at 40 $mJcm^{-2}$ and 100 pulses or 70 $mJcm^{-2}$ and 5 pulses. At these fluences, the temperature estimated by simulations at the film surface was above 300 °C for the five-layer film, close to the crystallization temperature reported for the sol-gel cerium oxide coatings. The crystallization into cubic cerium oxide was further corroborated by Raman spectroscopy.

Although it is complex to predict the origin of the different morphology, there are some general factors that can be considered. During pulse laser irradiation, the heat distribution is not uniform along the film thickness [39]. The amount of heat generated is influenced by the amount of laser photons absorbed in the film, expressed by the optical penetration depth ($l_\alpha = \alpha^{-1}$). From optical measurements, we estimated a penetration depth of about 200 nm (see Table S4); consequently, only half of the thickness of the 5L_$CeO_2$ sample is impacted by the process during the first pulse of irradiation. Numerical simulations confirm the presence of a large temperature gradient between the film surface and the interface in the case of the thick samples. In addition, a chemical transition to the metal-oxide phase occurs during ELA of sol-gel (as confirmed by FTIR measurements), causing a variation in the morphological, chemical and thermal properties that influences the laser-matter interaction during a multiple-pulse process.

Furthermore, the rapid heating and cooling cycle could introduce thermal stress in the material, resulting in material degradation [39]. For instance, spherical particles and partial removal of the one-layer film from the substrate could be caused by ablation or dewetting induced by thermal reflow [40, 41]. Indeed, heat accumulation during ELA with multiple pulses could lead to a temperature higher than that estimated for a single pulse-inducing material ablation. Similar morphologies were found on crystalline $CeO_2$ films (thermally annealed at 500 °C) after ELA at 100 $mJcm^{-2}$ and 1000 pulses (data not shown). Finally, light scattering phenomena caused by the increasing surface roughness can lead to the high absorption of the laser compared to the absorption of the initially smooth surface [3]. For instance, Charpentier et al. [42]. considered the morphological and microstructural modification of ZnO:Al sol-gel films above a certain fluence threshold as a consequence of a melting and recrystallization phenomenon, with a melted top layer of increasing thickness, by increasing the laser fluence.

Changes in cerium oxide morphology as a function of the layer thickness have been reported for magnetron-sputtered films. Lavkova et al. observed the formation of nonporous layers on graphite foil with a morphology changing from a smooth surface through a fractal-like character to hilly-like structures as the layer thickness increased [43]. De Jesus Acosta Silva et al. noted a variation of surface morphology of sol-gel cerium oxide films on glass substrates with annealing temperature. The film annealed at 250 °C was smooth, while films annealed at 450–550 °C showed a granular morphology [22]. Nanoporous granular morphology has been described for sol-gel films thermally annealed at 400 °C obtained by a water-based cerium nitrate solution dip coated onto ITO substrates [14]. It is worth noting that for the 5L_CeO2 film at 40 $mJcm^2$ and 100 pulses, we obtained a continuous crystalline film (see Fig. 6a) with a relative smooth surface (see Fig. 5d).

For the 5L_$CeO_2$ sample, the morphological evolution led to the formation of a 3D nanostructured surface, which shows a characteristic "rose effect" wettability, with high contact angle but significant contact angle hysteresis. This behavior was recently employed for the fabrication of water-transport surfaces by Li et al. In their work, they fabricated $CeO_2$ nanotubes through a hydrothermal method showing a prevalent (111) orientation, superhydrophobicity and pinning of water droplets. They explained the water-adhesion of the $CeO_2$ nanotube film as the combined effect of the van der Waals forces, the negative pressures produced by the sealed air and hydroxyl groups on the surface. Interestingly, the peculiar wetting behavior was durable even under UV irradiation and was easily restored by thermal annealing [23]. The use of laser annealing could be an alternative way for the fabrication of coatings with controlled wettability and be further explored for the fabrication of hydrophobicity gradients, as recently demonstrated for cerium oxide films prepared by magnetron sputtering [35].

## 5 Conclusions

In this manuscript we reported a preliminary investigation of the pulsed excimer laser annealing on sol-gel cerium oxide

films. XRD and Raman spectroscopy confirmed that ELA induced the formation of cubic cerium oxide. Threshold parameters for crystallization were found at 40 mJcm$^2$ and 100 pulses or 70 mJcm$^2$ and 5 pulses, which corresponded to an estimated temperature at the film surface in the range of 300–500 °C. The crystallization occurs with a morphological evolution with an increase in the surface nanostructuring by increasing the film thickness. ELA caused cracking and dewetting on one-layer films, while porous nanostructured films were achieved by increasing the number of pulses on five-layer films. Continuous crystalline films with a relatively smooth surface were obtained on five-layer samples at 40 mJcm$^2$ and 100 pulses. Although further work is required to reduce the cracking by controlling the temperature gradient inside the films, we expect that ELA could find application for the fabrication of nanostructured films on thermally-sensitive substrates for wettability-gradient surfaces or gas sensors.

**Supplementary information** The online version contains supplementary material available at https://doi.org/10.1007/s10971-023-06225-4.

**Acknowledgements** L. Bacci and N. Argiolas (University of Padova) are acknowledged for their precious technical assistance.

**Funding** This work was supported by the University of Padova through the grant UNIPD-ISR 2017 "SENSITISE" and through the SID project (BIRD221997) under the BIRD 2022 program. Open access funding provided by Università degli Studi di Padova.

## Compliance with ethical standards

**Conflict of interest** The authors declare no competing interest.



## References

1. Park JW, Kang BH, Kim HJ (2020) A Review of Low-Temperature Solution-Processed Metal Oxide Thin-Film Transistors for Flexible Electronics. Adv Funct Mater 30(40pp):1904632. https://doi.org/10.1002/adfm.201904632
2. Choi Y, Seong K-d PiaoY (2019) Metal−Organic Decomposition Ink for Printed Electronics. Adv Mater Interf 6(14pp):1901002. https://doi.org/10.1002/admi.201901002
3. Palneedi H, Park JH, Maurya D, Peddigari M, Hwang G-T, Annapureddy V, Kim J-W, Choi J-J, Hahn B-D, Priya S, Lee KJ, Ryu J (2018) Laser Irradiation of Metal Oxide Films and Nanostructures: Applications and Advances. Adv Mater 30(38pp):1705148. https://doi.org/10.1002/adma.201705148
4. Joya YF, Liu Z (2011) Effect of the excimer laser irradiation on sol-gel derived tungsten-titanium dioxide thin films. Appl Phys A Mater 102:91–97. https://doi.org/10.1007/S00339-010-6151-9
5. Winfield RJ, Koh LHK, O'Brien S, Crean GM (2007) Excimer laser processing of ZnO thin films prepared by the sol-gel process. Appl Surf Sci 254:855–858. https://doi.org/10.1016/j.apsusc.2007.08.072
6. Kim K, Kim S, Lee SY (2012) Effect of excimer laser annealing on the properties of ZnO thin film prepared by sol-gel method. Curr Appl Phys 12:585–588. https://doi.org/10.1016/j.cap.2011.09.006
7. Basso M, Colusso E, Carraro C, Kalha C, Riaz AA, Bombardelli G, Napolitani E, Chen Y, Jasieniak J, Ratcliff LE, Thakur PK, Lee TL, Regoutz A, Martucci A (2023) Rapid laser-induced low temperature crystallization of thermochromic VO2 sol-gel thin films. Appl Surf Sci 631(11pp):157507. https://doi.org/10.1016/j.apsusc.2023.157507
8. Dellis S, Isakov I, Kalfagiannis N, Tetzner K, Anthropoulos TD, Koutsogeorgis DC (2017) Rapid laser-induced photochemical conversion of sol–gel precursors to In2O3 layers and their application in thin-film transistors. J Mater Chem C Mater 5:3673–3677. https://doi.org/10.1039/c7tc00169j
9. Tsay CY, Huang TT (2013) Improvement of physical properties of IGZO thin films prepared by excimer laser annealing of sol–gel derived precursor films. Mater Chem Phys 140:365–372. https://doi.org/10.1016/j.matchemphys.2013.03.051
10. Tsay CY, Wang MC (2013) Structural and optical studies on sol–gel derived ZnO thin films by excimer laser annealing. Ceram Int 39:469–474. https://doi.org/10.1016/j.ceramint.2012.06.050
11. Tang WX, Gao PX (2016) Nanostructured cerium oxide: Preparation, characterization, and application in energy and environmental catalysis. MRS Commun 6:311–329. https://doi.org/10.1557/mrc.2016.52
12. Cho YJ, Jang H, Lee KS, Kim DR (2015) Direct growth of cerium oxide nanorods on diverse substrates for superhydrophobicity and corrosion resistance. Appl Surf Sci 340:96–101. https://doi.org/10.1016/j.apsusc.2015.02.138
13. Logothetidis S, Patsalas P, Charitidis C (2003) Enhanced catalytic activity of nanostructured cerium oxide films. Mater Sci Eng: C 23:803–806. https://doi.org/10.1016/j.msec.2003.09.081
14. özer N (2001) Optical properties and electrochromic characterization of sol–gel deposited ceria films. Sol Energ Mat Sol C 68:391–400. https://doi.org/10.1016/S0927-0248(00)00371-8
15. Li H, Qu Y, Zhang X (2021) The gas sensor utilizing CeO2 nanorods for the low temperature detection of hydrogen. Inorg Chem Commun 130(6pp):108692. https://doi.org/10.1016/j.inoche.2021.108692
16. Singh V, Draper R, Seal S (2013) Effect of Processing Parameters on Cerium Oxide Coating Deposition in Solution Precursor Plasma Spray. J Am Ceram Soc 96:2437–2444. https://doi.org/10.1111/jace.12436
17. Mansilla C (2009) Structure, microstructure and optical properties of cerium oxide thin films prepared by electron beam evaporation assisted with ion beams. Solid State Sci 11:1456–1464. https://doi.org/10.1016/j.solidstatesciences.2009.05.001
18. Murugan R, Vijayaprasath G, Ravi G (2015) The influence of substrate temperature on the optical and micro structural properties of cerium oxide thin films deposited by RF sputtering. Superlattices Microstruct 85:321–330. https://doi.org/10.1016/j.spmi.2015.05.041
19. Ishizaki T, Saito N (2010) Rapid formation of a superhydrophobic surface on a magnesium alloy coated with a cerium oxide film by a

simple immersion process at room temperature and its chemical stability. Langmuir 26:9749–9755. https://doi.org/10.1021/la100474x
20. Ansari AA, Kaushik A, Solanki PR, Malhotra BD (2008) Sol–gel derived nanoporous cerium oxide film for application to cholesterol biosensor. Electrochem Commun 10:1246–1249. https://doi.org/10.1016/j.elecom.2008.06.003
21. Pinar Gökdemir F, Evrim Saatci A, Özdemir O, Keskin B, Kutlu K (2015) Structural, optical and electrochromic properties of cerium dioxide thin films prepared by sol–gel dip coating method. Mater Sci Semicond Process 38:300–305. https://doi.org/10.1016/j.mssp.2014.08.037
22. De Jesus Acosta-Silva Y, Castañedo-Perez R, Torres-Delgado G, Arturo Méndez-López A, Zelaya-Ángel O (2017) Effect of annealing temperature on structural, morphological and optical properties of CeO2 thin films obtained from a simple precursor solution. J Solgel Sci Technol 82:20–27. https://doi.org/10.1007/s10971-016-4286-7
23. Li X-P, Sun Y-L, Xu Y-Y, Chao Z-S (2018) UV-Resistant and Thermally Stable Superhydrophobic CeO2 Nanotubes with High Water Adhesion. Small 14(11pp):1801040. https://doi.org/10.1002/smll.201801040
24. Houlihan NM, Carpenter MA (2020) Morpho-Butterfly Inspired Lamella-based Optical Sensors for Measuring Percent Level Concentrations of H2 and CO with Au and CeO2. MRS Adv 5:2043–2053. https://doi.org/10.1557/adv.2020.318
25. Nelson AT, Rittman DR, White JT, Dunwoody JT, Kato M, McCellan KJ (2014) An Evaluation of the Thermophysical Properties of Stoichiometric CeO2 in Comparison to UO2 and PuO2. J Am Ceram Soc 97:3652–3659. https://doi.org/10.1111/jace.13170
26. Matsubayashi Y, Nomoto J, Yamaguchi I, Tsuchiya T (2020) Control of the oxygen deficiency and work function of SrFeO3-: δ thin films by excimer laser-assisted metal organic decomposition. CrystEngComm 22:4685–4691. https://doi.org/10.1039/d0ce00442a
27. Balakrishnan G, Raghavan CM, Ghosh C, Divakar R, Mohandas E, Song Jung Il, Bae SI, Kim TG (2013) X-ray diffraction, Raman and photoluminescence studies of nanocrystalline cerium oxide thin films. Ceram Int 39:8327–8333. https://doi.org/10.1016/j.ceramint.2013.03.103
28. Schilling C, Hofmann A, Hess C, Ganduglia-Pirovano MV (2017) Raman spectra of polycrystalline $CeO_2$: a density functional theory study. J Phys Chem C 121:20834–20849. https://doi.org/10.1021/acs.jpcc.7b06643
29. Wu Z, Li M, Howe J, Meyer HM, Overbury SH (2010) Probing defect sites on ceo2 nanocrystals with well-defined surface planes by Raman spectroscopy and O2 adsorption. Langmuir 26:16595–16606. https://doi.org/10.1021/la101723w
30. Loridant S (2021) Raman spectroscopy as a powerful tool to characterize ceria-based catalysts. Catal Tod 373:98–111. https://doi.org/10.1016/j.cattod.2020.03.044
31. Weber WH, Hass KC, McBride JR (1993) Raman study of CeO2: second-order scattering, lattice dynamics, and particle-size effects. Phys rev B Condens Matter 48:178–185. https://doi.org/10.1103/physrevb.48.178
32. Crnjak Orel Z (1999) Spectroscopic Characterization of Sol-Gel Dip-Coating CeO2 and CeO2/ SnO2 Films. Appl Spectrosc 53:241–245. https://doi.org/10.1366/0003702991946389
33. Channei D, Nakaruk A, Phanichphant S, Koshy P, Sorrell SS (2013) Cerium dioxide thin films using spin coating. J Chem 2-4 (4pp). https://doi.org/10.1155/2013/579284
34. Simonenko TL, Simonenko NP, Mokrushin AS, Simonenko EP, Glumov OV, Mel'nikova NA, Murin IV, Kalinina MV, Shilova OA, Sevaastyanov VG, Kuznetsov NT (2020) Microstructural, electrophysical and gas-sensing properties of CeO2–Y2O3 thin films obtained by the sol-gel process. Ceram Int 46:121–131. https://doi.org/10.1016/j.ceramint.2019.08.241
35. Zhu D, Hu C, Zhao R, Tan X, Li Y, Mandić V, Shi Z, Zhang X (2022) Fabrication of cerium oxide films with thickness and hydrophobicity gradients. Surf Coat Technol 430(8pp):127985. https://doi.org/10.1016/j.surfcoat.2021.127985
36. Fronzi M, Assadi MHN, Hanaor DAH (2019) Theoretical insights into the hydrophobicity of low index CeO2 surfaces. Appl Surf Sci 478:68–74. https://doi.org/10.1016/j.apsusc.2019.01.208
37. Külah E, Marot L, Steiner R, Romanyuk A, Jung TA, Wäckerlin A, Meyer E (2017) Surface chemistry of rare-earth oxide surfaces at ambient conditions: reactions with water and hydrocarbons. Sci Rep 7(10pp):43369. https://doi.org/10.1038/srep43369
38. Chakraborty M, Weibel JA, Schaber JA, Garimella SV (2019) The Wetting State of Water on a Rose Petal. Adv Mater Interf 6:1900652. https://doi.org/10.1002/admi.201900652
39. Im TH, Lee JH, Wang HS, Sung SH, Kim YB, Rho Y, Grigoropoulos CP, Park JH, Lee KJ (2021) Flashlight-material interaction for wearable and flexible electronics. Mater Today 51:525–551. https://doi.org/10.1016/j.mattod.2021.07.027
40. Colusso E, Martucci A, Neto C (2019) Fabrication of Biomimetic Micropatterned Surfaces by Sol–Gel Dewetting. Adv Mater Interf 6:1801629. https://doi.org/10.1002/admi.201801629
41. Kwon SJ, Park JG (2006) Dewetting of a sol-gel-derived thin film. Langmuir 22:3895–3898. https://doi.org/10.1021/la0519655
42. Charpentier C, Boukhicha R, Prod'Homme P, Emeraud T, Lerat J-F, Roca i Cabarrocas R, Johnson EV (2014) Evolution in morphological, optical, and electronic properties of ZnO:Al thin films undergoing a laser annealing and etching process. Sol Energ Mat Sol C 125:223–232. https://doi.org/10.1016/j.solmat.2014.02.027
43. Lavkova J, Khalakhan I, Chundak M, Vorokhta M, Potin V, Matolin V, Matolinova I (2015) Growth and composition of nanostructured and nanoporous cerium oxide thin films on a graphite foil. Nanoscale 7:4038–4047. https://doi.org/10.1039/c4nr06550f